Ceramics International 46 (2020) 23257–23261

Contents lists available at ScienceDirect

Ceramics International

journal homepage: www.elsevier.com/locate/ceramint

Short communication

Unravelling the sintering temperature-induced phase transformations in Ba($Fe_{0.7}Ta_{0.3}$)$O_{3-\delta}$ ceramics

B. Mallesham[a], Vishal Zade[a], Aldo Rubio[a], Susheng Tan[b], Rahul Panat[c,**], C.V. Ramana[a,*]

[a] Centre for Advanced Materials Research (CMR), University of Texas at El Paso, 500 W University Ave, El Paso, TX, 79968, USA
[b] Department of Electrical and Computer Engineering, Petersen Institute of NanoScience and Engineering, University of Pittsburgh, 3700 O'Hara Street, Pittsburgh, PA, 15261, USA
[c] Department of Mechanical Engineering, Carnegie Mellon University, 5000 Forbes Ave., Pittsburgh, PA, 15213, USA

ARTICLE INFO

Keywords:
Ba($Fe_{0.7}Ta_{0.3}$)$O_{3-\delta}$
Crystal structure
Phase transformations
XRD
HRTEM

ABSTRACT

Our work reports on the fundamental details of the crystal structure and phase transformations in Ba($Fe_{0.7}Ta_{0.3}$)$O_{3-\delta}$, the best known temperature-independent oxygen-sensing ceramic material for applications in extreme environments. Ba($Fe_{0.7}Ta_{0.3}$)$O_{3-\delta}$ ceramics were synthesized using conventional solid-state ceramic reaction under variable sintering temperatures (T_s = 1200–1350 °C). Combined X-ray diffraction (XRD) and high-resolution transmission electron microscopy (TEM) measurements revealed the T_s-induced phase transformations and their origin in Ba($Fe_{0.7}Ta_{0.3}$)$O_{3-\delta}$. Associated with phase transformations, pseudo-cubic (PC) reflections, such as $\{200\}_{PC}$, $\{211\}_{PC}$, and $\{220\}_{PC}$, exhibited distinct anomalies with increasing T_s. At T_s = 1200 °C, Ba($Fe_{0.7}Ta_{0.3}$)$O_{3-\delta}$ stabilized in mixed orthorhombic + rhombohedral phases (Amm2 + R3m). With increasing T_s (≥1250 °C), Ba($Fe_{0.7}Ta_{0.3}$)$O_{3-\delta}$ ceramics stabilized in tetragonal/rhombohedral [P4mm + R3m] mixed phases, while variations in the quantity of the respective phases were observed. Because both structure and crystal chemistry play key roles in achieving enhanced performance in chemical sensing and catalytic converters, detailed understanding of the phase transformations and crystal structure of Ba($Fe_{0.7}Ta_{0.3}$)$O_{3-\delta}$ ceramics, as derived in this work, will be useful to develop chemical sensors with optimum performance for high-temperature and corrosive environments.

Advanced ceramic materials are used in a wide variety of optical, electrical, electro-optic, mechanical, magnetic, and magneto-electronic applications. One particular area of rapidly growing interest in advanced ceramics is green-energy and smart-transportation industrial technologies. Here, oxide ceramics are used for process optimization, resulting in enhanced efficiency and complete elimination of process-related environmental pollution [1–3]. In order to eliminate undesirable emissions that negatively affect air quality, reliable and rapid-response sensors are required. Simple and multi-component oxide ceramics are key functional components of these sensors used to monitor and control a wide variety of hazardous chemicals [1–4]. In recent years, the demand for fast and reliable sensors based on relatively inexpensive oxide ceramics that are robust, lightweight, highly sensitive, selective, and exhibit long-term shelf lives has been rising exponentially [1,2,5–8].

Intrinsic and doped oxides based on Sn, Ti, Ce, W, In and Ga have been thoroughly investigated [1–12] for the design and development of various sensors for direct integration into energy, electronics, and transportation related industrial applications. These oxides respond to variations in oxygen partial pressure by maintaining the equilibrium between surrounding oxygen and ionic and/or electronic defects present in these oxides [2,6,9,11]. Sensors fabricated using oxide ceramics take a simple design, are inexpensive, and exhibit very good sensing performance. However, significant interference of temperature while operating in exhaust emissions is a major drawback of most oxide ceramics [13]. Perovskite oxide ceramics, such as doped Sr, Ba, and Ca-based materials ($SrTiO_3$, $BaTiO_3$, $CaTiO_3$), have been considered as new materials for oxygen sensor applications [14–19]. Because of their high melting point and decomposition temperature, perovskite oxide ceramics are particularly attractive for high-temperature sensor applications [14–19]. Perovskite oxide ceramics – with a general formula of ABO_3 – contain two differently sized cations at sites A and B, which allows doping of different cations. The ability to use different dopants facilitates tuning of structure and defect chemistry, which in turn offers

* Corresponding author.
** Corresponding author.
E-mail addresses: rpanat@andrew.cmu.edu (R. Panat), rvchintalapalle@utep.edu (C.V. Ramana).

https://doi.org/10.1016/j.ceramint.2020.04.124
Received 9 November 2019; Received in revised form 15 March 2020; Accepted 12 April 2020
Available online 20 April 2020
0272-8842/ © 2020 Elsevier Ltd and Techna Group S.r.l. All rights reserved.

control of electrical transport and catalytic properties [17–21]. Thus, manipulating the structure-property relationship by means of A, B cation doping readily allows optimization of sensor performance for desired technological application.

The emergence of two selected material systems (both based on Fe-doped oxides, $SrTi_{1-x}Fe_xO_3$ (STF) and $BaFe_{1-y}Ta_yO_3$ (BFT)) [17–19,22] drove the development of temperature independent oxygen sensors based on perovskite oxide ceramics [19,22]. While there were some concerns and debate about the temperature independence of the sensor behavior of STF [17], $Ba(Fe_{1-x}Ta_x)O_{3-\delta}$ (BFTO) has been confirmed as a temperature-independent oxygen sensor material that functions over a broad ranges in temperature and oxygen partial pressure [19,22]. In particular, it has been demonstrated that the specific composition $Ba(Fe_{0.7}Ta_{0.3})O_{3-\delta}$ exhibits rapid and stable response to very high temperature (~900 °C) [19,22,23]. However, no major efforts have been made to understand the fundamental scientific aspects of the effect of temperature on crystal structure and phase transformation in BFTO.

The performance of oxide ceramics is determined by a number of material characteristics, including purity, homogeneity, particle size and shape, and chemistry, which in turn depend on the starting ingredients and their respective purity and synthetic conditions. The crystal structure and the phase of the resulting oxide ceramic materials in particular depend on processing conditions and method of preparation. Optimizing the structure and phase of a given oxide ceramic can significantly improve the sensing parameters, such as sensitivity, stability, and selectivity [9,24]. In this context, our work focused on deriving a comprehensive understanding of phase transformations, phase coexistence (if any), and crystal structure of $Ba(Fe_{0.7}Ta_{0.3})O_{3-\delta}$ ceramics made by the standard high-temperature, solid-state ceramic method. Interestingly, as presented and described in this communication, we demonstrated for the first time that the sintering temperature induces phase transformations in $Ba(Fe_{0.7}Ta_{0.3})O_{3-\delta}$ ceramics and that optimization of a specific phase and crystal structure is possible by tuning the ceramic processing conditions.

$Ba(Fe_{0.7}Ta_{0.3})O_{3-\delta}$ [BFTO30] compounds were synthesized using the conventional high-temperature, solid-state chemical reaction method. High purity precursor materials, namely $BaCO_3$ (99.9%, Sigma Aldrich), Fe_2O_3 (99.9%, Sigma Aldrich), and Ta_2O_5 (99.9%, Sigma Aldrich), were weighed in stoichiometric proportions to achieve the desired compound. Stoichiometrically weighed precursors were homogeneously ground in an agate mortar using acetone as wetting medium. Homogeneously ground powders were calcined at different temperatures (1000 °C, 1050 °C, 1100 °C, and 1150 °C) with intermediate grinding to achieve phase purity. Calcined powders were reground to decrease particle size; fine powder was pelletized using a die and uniaxial hydraulic press by applying a load of 1.5 ton in the form of circular disc (8 mm diameter and 1 mm thickness). Pellets were sintered in a muffle furnace at different sintering temperatures (T_s) of 1200 °C, 1250 °C, 1300 °C, and 1350 °C.

X-ray diffraction (XRD) measurements were made using a Rigaku X-ray diffractometer (Mini Flex II). Both calcined and sintered compounds were analyzed at room temperature. The XRD parameters employed were: 10°–80° (2θ range), step size 0.02°, and scan rate 0.6°/min. Measurements were made so as to obtain appreciable intensities that are useful to refine the XRD patterns using the well-known Rietveld method, which was also useful to estimate the specific compound. The transmission electron microscopy measurements (JEOL JEM-2100F TEM equipped with Oxford AZtec energy dispersive X-ray spectrometer and Gatan Tridiem GIF electron energy loss spectrometer) were made to analyze the surface morphology and crystal symmetry of the BFTO samples. Bright field images and selected area electron diffraction (SAED) patterns were recorded. In order to prepare TEM samples, a small amount of sintered powder was diluted with ethanol, the suspension was sonicated, and a single drop of the resulting suspension was placed on a carbon-coated copper grid and allowed to dry in air.

Fig. 1 shows the XRD patterns of $Ba(Fe_{0.7}Ta_{0.3})O_{3-\delta}$ sintered at different temperatures. The BFTO samples stabilized in perovskite phase without any phase separation, even at high temperatures. The crystallite sizes for BFTO samples sintered at different temperatures was estimated using the Debye Scherrer relation [25]:

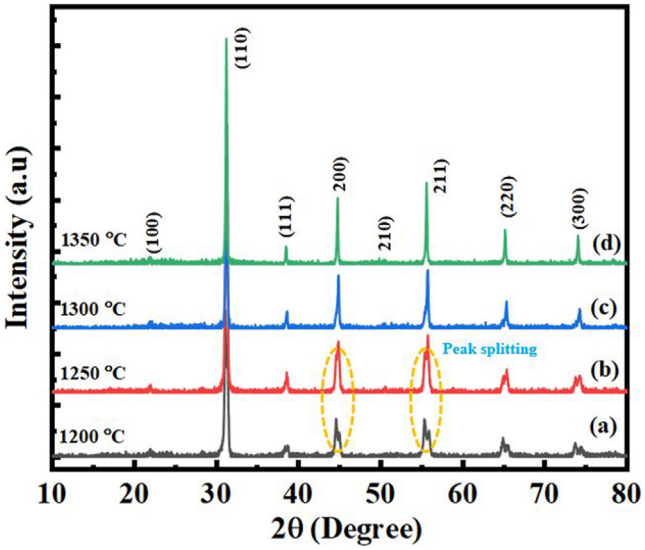

Fig. 1. X-ray diffraction patterns of $Ba(Fe_{0.7}Ta_{0.3})O_{3-\delta}$ compounds sintered at different temperatures. The peaks identified are as indexed.

$$D_{hkl} = \frac{0.9\lambda}{\beta \cos\theta} \quad (1)$$

where D is the crystallite size, λ ($Cu_{K\alpha}$) - 1.5406 Å, β is the full width at half maximum, and θ is the diffraction angle. The crystallite size increased from ~24 nm to ~80 nm with sintering temperatures increasing from 1200 °C to 1350 °C.

The stability and symmetry of the perovskite structure was determined by Goldschmidt's tolerance factor (*t*) [26] based on the chemical formula given by:

$$t = \frac{R_A + R_O}{\sqrt{2}\,(R_B + R_O)} \quad (2)$$

where R_A and R_B are the ionic radii of A-site and B-site cations, and R_O is the ionic radius of oxygen. The Shannon ionic radii [27] of the constituent elements are: 1.61 Å (Ba^{2+}), 0.64 Å (Ta^{5+}), 0.645 Å (Fe^{3+}, high-spin state), 0.55 Å (Fe^{3+}, low-spin state), and 1.4 Å (O^{2-}). The estimated tolerance factor values for Fe^{3+} high-spin and low-spin states are 1.07 and 1.11, respectively. The estimated tolerance factor value shows that the synthesized BFTO compound stabilized in either hexagonal or tetragonal phase as a result of the significant difference between A-site and B-site ionic radii.

Interestingly, clear peak splitting (as indicated by orange dotted lines in Fig. 1) is evident in samples sintered at 1200 °C and 1250 °C; however, such peak splitting almost vanished in BFTO samples sintered at 1350 °C. Fig. 2 represents the magnified profiles of pseudo-cubic $\{200\}_{PC}$, $\{211\}_{PC}$, and $\{220\}_{PC}$ reflections; subscript PC indicates diffraction peaks are indexed using pseudo-cubic symmetry. As can be seen in Fig. 2, increasing T_s resulted in variation of splitting feature and their intensity ratio, both clear evidence of the structural transformations in BFTO30 with varying sintering temperature. All reflections of BFTO samples sintered at 1200 °C exhibited doublet characteristics. The splitting behavior of the $\{200\}_{PC}$ reflection revealed tetragonal crystal symmetry; however, for pure tetragonal phase the intensity ratio of $I_{(002)}/I_{(200)} \approx 0.5$ (the (002) reflection corresponded to a lower Bragg angle while the (200) reflection corresponded to a higher Bragg angle) [28]. The observed intensity ratio between lower and higher Bragg angle peaks of $\{200\}_{PC}$ for BFTO sintered at 1200 °C was ≈1.6, which indicated a lack of tetragonal phase stability of these BFTO samples.

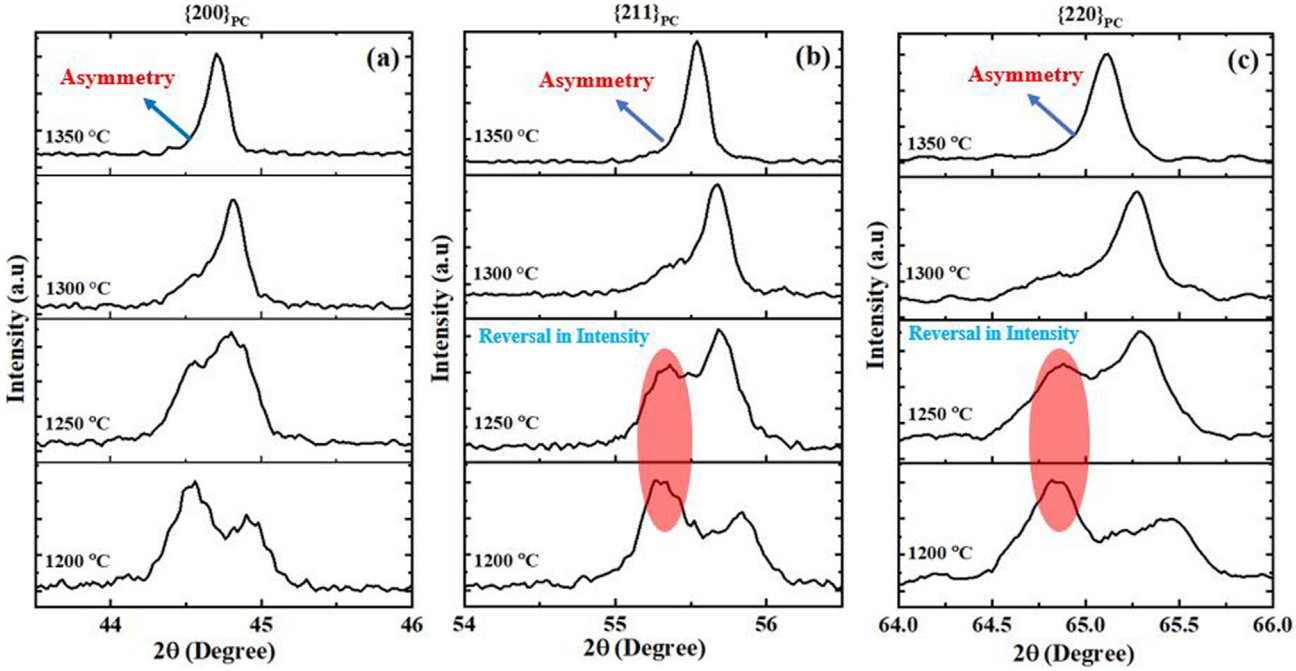

Fig. 2. Magnified pseudo-cubic reflections of samples sintered at different temperatures (a) $\{200\}_{PC}$, (b) $\{211\}_{PC}$, and (c) $\{220\}$.

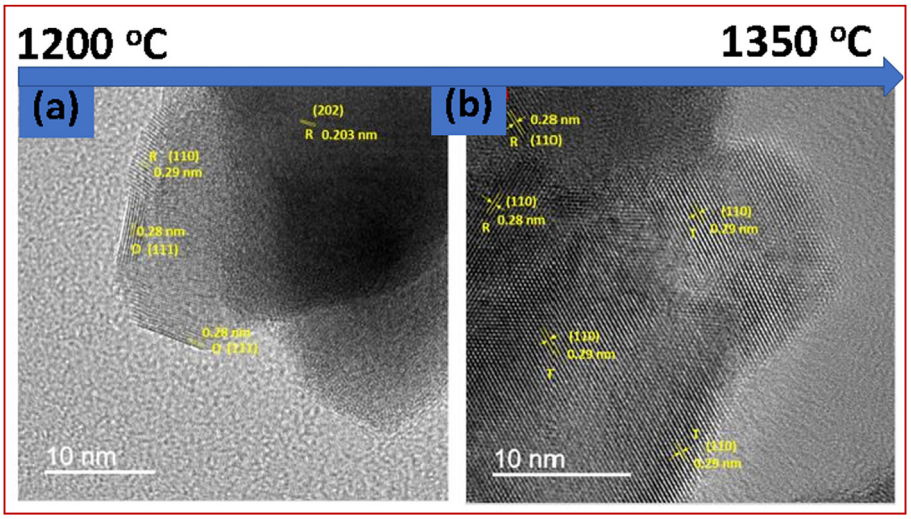

Fig. 3. HRTEM images of samples sintered at different temperatures. The images shown are for samples sintered at: (a) 1200 ˚C and (b) 1350 ˚C.

Moreover, for the pure rhombohedral phase, the (200) peak should have been a singlet; however, the observed doublet characteristics revealed an absence of the rhombohedral phase. The observed features of the (200) reflection, such as clear splitting and an intensity ratio of $I_{(022)}/I_{(200)} \approx 1.6$ were very similar to the orthorhombic phase [28]. The broadening of $\{211\}_{PC}$ and $\{220\}_{PC}$ was attributed to the presence of more than two peaks, which resulted from orthorhombic symmetry. Similar characteristic features of pseudo-cubic reflections were also reported in doped-$BaTiO_3$ compounds and confirmed that the features were associated with the resultant of mixed phases, such as orthorhombic + rhombohedral or orthorhombic + tetragonal [28–31]. Preliminary peak analysis showed that BFTO samples sintered at 1200 ˚C may have stabilized in orthorhombic or mixed phase.

BFTO samples sintered at 1250 ˚C showed marked differences compared to those sintered at 1200 ˚C, in particular in their XRD peak behavior. The pseudo-cubic profiles $\{200\}_{PC}$, $\{211\}_{PC}$, and $\{220\}_{PC}$ exhibited a reversal in the intensity of split peaks (indicated by red ovals in Fig. 2). In addition to this intensity reversal, the $\{200\}_{PC}$ reflection exhibited more distinct characteristics, such as an absence of clear splitting, and anomalous broadening with a small shoulder peak at lower Bragg angle. These features are evidence of the structural transformation in BFTO30 with increasing sintering temperature. The reversal in peak intensity with sintering temperature increasing from 1200 ˚C to 1250 ˚C may be attributed to the phase transition from a orthorhombic to tetragonal structure [28,29]. In BFTO samples sintered at 1300 ˚C, the splitting of pseudo-cubic reflections disappeared, and peaks became highly asymmetric. The $\{200\}_{PC}$ reflection exhibited a small shoulder at lower Bragg angle, while broader shoulders for $\{211\}_{PC}$ & $\{220\}_{PC}$ reflections were observed. The noticeable changes between 1250 ˚C and 1300 ˚C can only be attributed to either structural transition or fraction of phase change. For samples sintered at 1350 ˚C, the pseudo-cubic reflections represented in Fig. 2 exhibited singlet features which indicated that the compound sintered at 1350 ˚C stabilized in cubic phase. However, closer examination of the reflections confirmed an asymmetry at lower Bragg angle along with singlet-like features. These features can be attributed to stabilization of the

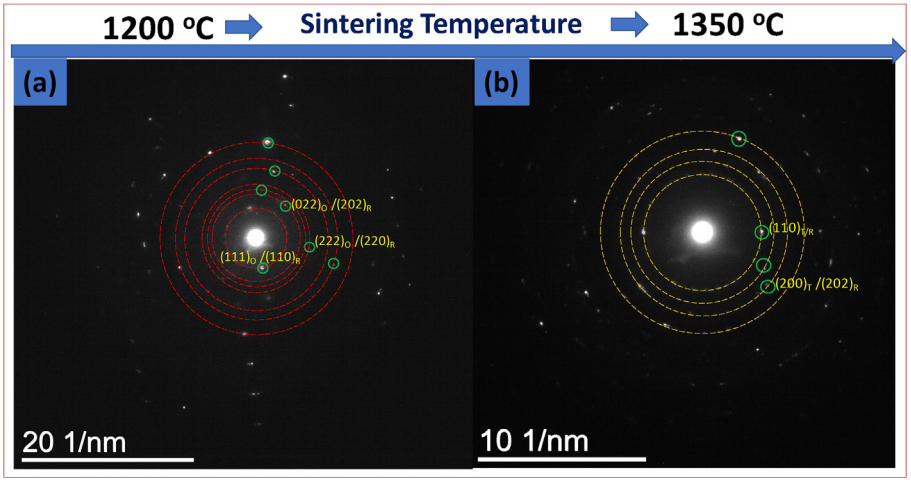

Fig. 4. Selected area electron diffraction pattern of BFTO samples sintered at different temperatures. The images shown are for samples sintered at: (a) 1200 ˚C and (b) 1350 ˚C.

compound in rhombohedral phase (closest structure to cubic phase). Further analyses of the XRD data using theoretical considerations and refinements (not shown) indicated that the tetragonal (*P4mm*) phase decreases gradually from 34.5% to 12.6% with increasing sintering temperature from 1200 to 1350 ˚C. Correspondingly, the rhombohedral (*R3m*) phase increases gradually from 65.5% to 87.4% with increasing sintering temperature from 1200 to 1350 ˚C. The substantial changes in percentage of the different crystal symmetries in BFTO30 can only be due to the effect of sintering temperature, which induces phase transformations and a well-defined phase-transformation-sequence.

To further confirm and validate the phase coexistence and structural transformation of BFTO compounds as a function of T_s, HRTEM imaging analysis of the samples was performed. Fig. 3 represents the HRTEM images of the sintered BFTO samples. Distinct lattice fringes with different lattice spacing are evident in all samples. Lattice fringes of one orientation are diffused into other, a clear lattice boundary layer was absent. However, interplanar distances (*d*-spacing) calculated from the HRTEM images are as represented in Fig. 3. The calculated interplanar spacing values were corroborated satisfactorily by crystallographic analysis made using XRD. It was evident that *d*-spacing values corresponded to lattice fringes of two phases that were closely matched because of very similar lattice parameters. However, lattice fringes correspond to two different phases unambiguously, as represented based on *d*-spacing values.

Fig. 4 shows the corresponding selected area electron diffraction (SAED) patterns of samples sintered at different T_s. The observed multiple, random diffraction spots (rings) are evidence of the coexistence of two different phases. Few reflections were indexed based on satisfactory crystallographic models Amm2 + R3m [1200 ˚C, Fig. 4 (a)] and Amm2 + R3m [1350 ˚C; Fig. 4 (b), respectively]. However, diffraction spots corresponded to two phases that were indistinguishable because of closely matched lattice spacing values.

1. Conclusions

Temperature-independent sensor materials based on $Ba(Fe_{0.7}Ta_{0.3})O_{3-\delta}$ compounds were synthesized using the conventional solid state reaction route and the effect of sintering temperature on crystal symmetry, phase coexistence, and phase transformations was determined. X-ray diffraction analyses revealed the evidence of structural transformations with increasing sintering temperature. At 1200 ˚C, the BFTO compounds stabilized in a mixed phase of orthorhombic (Amm2) and rhombohedral (R3m). Structural analyses confirmed the stabilization of a tetragonal (P4mm) and rhombohedral (R3m) mixed phase in BFTO compounds with sintering temperature increasing to 1250–1350 ˚C. As the sintering temperature increased, the fraction of tetragonal phase gradually decreased while the rhombohedral phase gradually increased. HRTEM revealed that the estimated *d*-spacings corresponded well with constituent phases of the respective compound.

Declaration of competing interest

The authors declare that they have no known competing financial interests or personal relationships that could have appeared to influence the work reported in this paper.

Acknowledgments

The authors at the University of Texas at El Paso acknowledge, with pleasure, support by the National Science Foundation (NSF) with NSF-PREM grant #DMR-1827745. This material is also based on work supported by the U.S. Department of Energy, National Energy Technology Laboratory (NETL), under Grant No. DE-FE0026170. However, any opinions, finding, or conclusions or recommendations expressed in this material are those of the author(s) and do not necessarily reflect the views of the Department of Energy. CVR and AR also acknowledges the support from US Department of Transportation through the Center for Transportation, Environment, and Community Health (CTECH). However, the contents of this report reflect the views of the authors, who are responsible for the facts and the accuracy of the information presented herein. This document is disseminated in the interest of information exchange. The report is funded, partially or entirely, by a grant from the U.S. Department of Transportation's University Transportation Centers Program. However, the U.S. Government assumes no liability for the contents or use thereof.

Appendix A. Supplementary data

Supplementary data to this article can be found online at https://doi.org/10.1016/j.ceramint.2020.04.124.

References

[1] G. Eranna, B. Joshi, D. Runthala, R. Gupta, Oxide materials for development of integrated gas sensors - a comprehensive review, Crit. Rev. Solid State Mater. Sci. 29 (2004) 111–188, https://doi.org/10.1080/10408430490888977.
[2] A. Dey, Semiconductor metal oxides gas sensors: a review, Mater. Sci. Eng. B 229 (2018) 206–217, https://doi.org/10.1016/j.mseb.2017.12.036 2018.
[3] Y. Mo, T. Liu, C. Wang, A limiting current oxygen sensor based on $(La_{0.4}Ce_{0.6}O_{2-\delta})_{0.96}(FeO_{1.5})_{0.04}$ as dense diffusion barrier, Ceram. Int. 45 (2019) 8319–8324, https://doi.org/10.1016/j.ceramint.2019.01.139.

[4] D. Han, Sol-gel autocombustion synthesis of zinc oxide foam decorated with holes and its use as acetic acid gas sensor at sub-ppm level, Ceram. Int. 46 (2019) 3304–3310, https://doi.org/10.1016/j.ceramint.2019.10.036.

[5] A. Elger, J. Baranyai, K. Hofmann, C. Hess, Direct operando spectroscopic observation of oxygen vacancies in working ceria-based gas sensors, ACS Sens. 4 (2019) 1497–1501, https://doi.org/10.1021/acssensors.9b00521.

[6] J. Bai, B. Zhou, Titanium dioxide nanomaterials for sensor applications, Chem. Rev. 114 (2014) 10131–10176, https://doi.org/10.1021/cr400625j.

[7] V.B. Kamble, A.M. Umarji, Correlating defect induced ferromagnetism and gas sensing properties of undoped tin oxide sensors, Appl. Phys. Lett. 104 (2014) 251912, https://doi.org/10.1063/1.4885424.

[8] E. Comini, Metal oxide nanowire chemical sensors: innovation and quality of life, Mater. Today 19 (2016) 559–567, https://doi.org/10.1016/j.mattod.2016.05.016.

[9] Y. Lu, Y. Ma, S. Ma, S. Yan, Hierarchical heterostructure of porous NiO nanosheets on flower-like ZnO assembled by hexagonal nanorods for high-performance gas sensor, Ceram. Int. 43 (2017) 7508–7515, https://doi.org/10.1016/j.ceramint.2017.03.032.

[10] N. Izu, W. Shin, I. Matsubara, N. Murayama, Development of resistive oxygen sensors based on cerium oxide thick film, J. Electroceram. 13 (2004) 703–706, https://doi.org/10.1007/s10832-004-5179-7.

[11] H. Kim, C. Jin, S. An, C. Lee, Fabrication and CO gas-sensing properties of Pt-functionalized Ga2O3 nanowires, Ceram. Int. 38 (2015) 3563–3567, https://doi.org/10.1016/j.ceramint.2011.12.072.

[12] D. Wang, Y. Lou, R. Wang, P. Wang, N. Jiang, Humidity sensor based on Ga_2O_3 nanorods doped with Na^+ and K^+ from GaN powder, Ceram. Int. 41 (2015) 14790–14797, https://doi.org/10.1016/j.ceramint.2015.07.211.

[13] K. Sahner, J. Straub, R. Moos, Cuprate-ferrate compositions for temperature independent resistive oxygen sensors, J. Electroceram. 16 (2006) 179–186, https://doi.org/10.1007/s10832-006-6203-x.

[14] J.W. Fergus, Perovskite oxides for semiconductor-based gas sensors, Sensor. Actuator. B Chem. 123 (2007) 1169–1179, https://doi.org/10.1016/j.snb.2006.10.051.

[15] C. Argirusis, F. Jomard, S.F. Wagner, W. Menesklou, E. Ivers-Tiffée, Study of the oxygen incorporation and diffusion in $Sr(Ti_{0.65}Fe_{0.35})O_3$ ceramics, Solid State Ionics 192 (2011) 9–11, https://doi.org/10.1016/j.ssi.2010.02.016.

[16] M. Fleischer, H. Meixner, Selectivity in high-temperature operated semiconductor gas-sensors, Sensor. Actuator. B Chem. 52 (1998) 179–187, https://doi.org/10.1016/S0925-4005(98)00271-8.

[17] A. Rothschild, S.J. Litzelman, H.L. Tuller, W. Menesklou, T. Schneider, E. Ivers-Tiffée, Temperature-independent resistive oxygen sensors based on $SrTi_{1-x}Fe_xO_{3-\delta}$ solid solutions, Sensor. Actuator. B Chem. 108 (2005) 223–230, https://doi.org/10.1016/j.snb.2004.09.044.

[18] C.L. Chow, W.C. Ang, M.S. Tse, O.K. Tan, Oxygen-sensing property of sol-gel derived $SrTi_{1-x}Fe_xO_{3-\delta}$ thin films with different iron concentrations (x = 0.2-0.8), Thin Solid Films 542 (2013) 393–398, https://doi.org/10.1016/j.tsf.2013.06.078.

[19] M. Bektas, D. Schönauer-Kamin, G. Hagen, A. Mergner, C. Bojer, S. Lippert, W. Milius, J. Breu, R. Moos, $BaFe_{1-x}Ta_xO_{3-\delta}$ - a material for temperature independent resistive oxygen sensors, Sensor. Actuator. B Chem. 190 (2014) 208–213, https://doi.org/10.1016/j.snb.2013.07.106.

[20] A. Rothschild, W. Menesklou, H.L. Tuller, E. Ivers-Tiffée, Electronic structure, defect chemistry, and transport properties of $SrTi_{1-x}Fe_xO_{3-y}$ solid solutions, Chem. Mater. 18 (2006) 3651–3659, https://doi.org/10.1021/cm052803x.

[21] H.D. Zhou, J.B. Goodenough, Polaron morphologies in $SrTi_{1-x}Fe_xO_{3-\delta}$, J. Solid State Chem. 177 (2004) 1952–1957, https://doi.org/10.1016/j.jssc.2004.01.015.

[22] R. Moos, N. Izu, F. Rettig, S. Rei, W. Shin, I. Matsubara, Resistive oxygen gas sensors for harsh environments 11 (2011), p. 3439, https://doi.org/10.3390/s110403439.

[23] M. Bektas, D. Hanft, D. Schönauer-Kamin, T. Stöcker, G. Hagen, R. Moos, aerosol-deposited $BaFe_{0.7}Ta_{0.3}O_{3-\delta}$ for nitrogen monoxide and temperature-independent oxygen sensing, J. Sens. Sens. Syst. 3 (2014) 223–229, https://doi.org/10.5194/jsss-3-223-2014.

[24] G. Korotcenkov, Gas response control through structural and chemical modification of metal oxide films: state of the art and approaches, Sensor. Actuator. B Chem. 107 (2005) 209–232, https://doi.org/10.1016/j.snb.2004.10.006.

[25] B.D. Cullity, S.R. Stock, Elements of X-Ray Diffraction, Prentice Hall, 2011.

[26] X.C. Liu, R. Hong, C. Tian, Tolerance factor and the stability discussion of ABO_3-type Ilmenite, J. Mater. Sci. Mater. Electron. 20 (2009) 323–327, https://doi.org/10.1007/s10854-008-9728-8.

[27] R.D. Shannon, Revised effective ionic radii and systematic studies of interatomic distances in halides and chalcogenides, Acta Crystallogr. A 32 (1976) 751–757, https://doi.org/10.1107/S0567739476001551.

[28] S. Dwivedi, T. Pareek, S. Kumar, Structure, dielectric, and piezoelectric properties of $K_{0.5}Na_{0.5}NbO_3$-based lead-free ceramics, RSC Adv. 8 (2018) 24286–24296, https://doi.org/10.1039/C8RA04038A.

[29] B.C. Keswani, R.S. Devan, R.C. Kambale, A.R. James, S. Manandhar, Y.D. Kolekar, C.V. Ramana, Correlation between structural, magnetic and ferroelectric properties of Fe-Doped (Ba-Ca)TiO_3 lead-free piezoelectric, J. Alloys Compd. 712 (2018) 320–333, https://doi.org/10.1016/j.jallcom.2017.03.301.

[30] B.C. Keswani, S.I. Patil, A.R. James, Y.D. Kolekar, C.V. Ramana, Correlation between structural, ferroelectric, piezoelectric and dielectric properties of $Ba_{0.7}Ca_{0.3}TiO_3$-$xBaTi_{0.8}Zr_{0.2}O_3$ (x = 0.45, 0.55) ceramics, Ceram. Int. 44 (2018) 20921–20928, https://doi.org/10.1016/j.ceramint.2018.06.115.

[31] L.F. Zhu, B.P. Zhang, L. Zhao, S. Li, Y. Zhou, X.C. Shi, N. Wang, Large piezoelectric effect of (Ba,Ca)TiO_3–x$Ba(Sn,Ti)O_3$ lead-free ceramics, J. Eur. Ceram. Soc. 36 (2016) 1017–1024, https://doi.org/10.1016/j.jeurceramsoc.2015.11.039.